available at www.sciencedirect.com

ScienceDirect

journal homepage: www.sciencedirect.com/journal/chinese-journal-of-catalysis

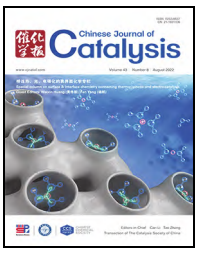

Article

Unveiling the active sites of ultrathin Co-Fe layered double hydroxides for the oxygen evolution reaction

Xue Bai [a,†], Zhiyao Duan [b,†,#], Bing Nan [c,†], Liming Wang [d], Tianmi Tang [a], Jingqi Guan [a,*]

[a] *Institute of Physical Chemistry, College of Chemistry, Jilin University, Changchun 130021, Jilin, China*

[b] *State Key Laboratory of Solidification Processing, School of Materials Science and Engineering, Northwestern Polytechnical University, Xi'an 710072, Shaanxi, China*

[c] *Shanghai Synchrotron Radiation Facility, Shanghai Advanced Research Institute, Chinese Academy of Science, Shanghai 201210, China*

[d] *CAS Key Laboratory for Biomedical Effects of Nanomaterials and Nanosafety & CAS-HKU Joint Laboratory of Metallomics on Health and Environment, Institute of High Energy Physics, Chinese Academy of Sciences, Beijing 100049, China*

ARTICLE INFO

Article history:
Received 28 December 2021
Accepted 31 January 2022
Available online 20 June 2022

Keywords:
Cobalt hydroxide
Iron hydroxide
Layered double hydroxide
Oxygen evolution reaction
First-principle study

ABSTRACT

Two-dimensional layered double hydroxides (LDHs) have been identified as promising electrocatalysts for the oxygen evolution reaction (OER); however, the simple and effective synthesis of high-quality LDHs remains extremely challenging and the active sites have not been clarified. Herein, we report a facile solution-reaction method for preparing an ultrathin (thickness < 2 nm) non-precious CoFe-based LDH. $Co_1Fe_{0.2}$ LDH delivers a current density of 10 mA cm^{-2} and a high turnover frequency of 0.082 s^{-1} per total 3d metal atoms at a low overpotential of 256 mV. Its mass activity is 277.9 A g^{-1} at an overpotential of 300 mV for the OER. Kinetic studies reveal the Co site as the main active center for the OER. The doped Fe lowers the reaction barrier by accelerating the charge-transfer process. Theoretical calculations reveal that the surface Co sites adjacent to Fe atoms are the active centers for the OER and the subsurface Fe dopants excessively weaken the OH* adsorption, thus increasing the energy barrier of the rate-determining step. This study can guide the rational design of high-performance CoFe-based LDHs for water splitting.

© 2022, Dalian Institute of Chemical Physics, Chinese Academy of Sciences.
Published by Elsevier B.V. All rights reserved.

1. Introduction

High-purity hydrogen produced by alkaline-water splitting (a renewable energy supply) offers a promising route toward sustainable energy and environmental development [1–5]. However, the kinetics of the electrocatalytic oxygen evolution reaction (OER) is very slow and the high energy barriers can only be overcome by large overpotentials that greatly degrade the energy efficiency [6–8]. First-class OER electrocatalysts have thus far been limited to noble Ir/Ru oxides [9,10], which are scarce and expensive and therefore unsuitable for industrial implementations. The development of cost-efficient OER catalysts with high electrocatalytic performance is highly demanded for hydrogen generation [11–13].

To replace Ru/Ir oxides with high-performance, earth-abundant catalysts for the OER, researchers have explored heterogeneous transition-metal oxides, (oxy)hydroxides, carbide, nitrides, halogenides, dichalcogeni-

* Corresponding author. E-mail: guanjq@jlu.edu.cn
# Corresponding author. E-mail: zhiyao.duan@nwpu.edu.cn
† Contributed equally to this work.

This work was supported by the National Natural Science Foundation of China (22075099), the Education Department of Jilin Province (JJKH20220967KJ), and the Fundamental Research Funds for the Central Universities (D5000210743).
DOI: 10.1016/S1872-2067(21)64033-0 | http://www.sciencedirect.com/journal/chinese-journal-of-catalysis | Chin. J. Catal., Vol. 43, No. 8, August 2022

(C)1994-2023 China Academic Journal Electronic Publishing House. All rights reserved. http://www.cnki.net

des, selenides, and phosphides [14–16]. Although these compounds achieve high OER activity, only transition-metal oxides and (oxy)hydroxides are stable toward the oxygen evolution process; the others ultimately transform into their corresponding oxides [17,18]. Therefore, it is highly desirable to design and synthesize transition-metal oxides and (oxy)hydroxides for the OER from the viewpoint of practical applications. In recent years, CoFe-based oxides and (oxy)hydroxides have emerged as highly active and stable OER electrocatalysts with performances comparable to those of NiFe-based (oxy)hydroxides and precious metal oxides [19]. A variety of structures have been constructed, including nanoparticles (NPs) [20], nanosheets [21], core-shell structures [22], amorphous structures [23], mesoporous structures [24], and crystalline structures [25,26]. Owing to their unique two-dimensional (2D) structure and tunable chemical composition, CoFe layered double hydroxides (LDHs) exhibit excellent OER activity in alkaline media. However, CoFe LDHs have lower OER activity than Ru/Ir-based catalysts because the overall structure of LDHs is difficult to control and their active sites are unevenly distributed. The rational design and preparation of CoFe LDHs with an ultrathin structure would expose more active sites and homogeneously disperse the Fe and Co sites, thus accelerating the electron transport. This solution appears to be the key for improving the OER performance.

Although considerable efforts have been devoted for characterizing and understanding the structural and electronic properties of CoFe LDHs, the OER catalytic sites of CoFe LDHs remain contentious. The OER active centers have been identified as (1) Fe sites, (2) Co sites, (3) *di*-μ-oxo-bridged Fe-Co sites, and (4) oxygen vacancies. Yeo *et al*. [27] performed an in situ X-ray absorption fine structure (XAFS) characterization of CoO_x and concluded that Fe sites with oxygen vacancies are involved in the OER activity enhancement of CoO_x. Using time-resolved in situ X-ray absorption, Smith *et al*. [28] found that the OER predominantly occurs at *di*-μ-oxo-bridged Co-Co and *di*-μ-oxo-bridged Fe-Co sites. Wang *et al*. [29] reported that introducing defects can increase the number of dangling bonds adjacent to the reactive sites and reduce the coordination number of these sites. Zhu *et al*. [21] found that oxygen vacancies can boost the electronic conductivity and accelerate the adsorption of water at Co^{3+} sites. To date, there is no substantial evidence that would unify the experimental and theoretical results and thus reveal the true active sites of CoFe LDHs for the OER. To acquire this knowledge, we conducted a systematic comparison between a range of CoFe LDHs synthesized using the same method. Specifically, we measured their kinetic barriers and compared the results with the theoretical overpotentials on different LDH sites. We found that the Co sites adjacent to surface Fe atoms are the oxygen evolution centers and large overpotentials are required on Fe sites.

2. Experimental

2.1. Materials

All the chemicals were used without further purification and the water used was deionized water (DIW). $Co(NO_3)_2{\cdot}6H_2O$ (98.5%), $FeCl_3{\cdot}6H_2O$ (99.9%), sodium borohydride ($NaBH_4$, > 99%), and C_2H_5OH (> 99.7%) were obtained from Sinopharm Chemical Reagent. PEG-PPG-PEG (Pluronic P123, > 95%) was purchased from Alfa Aesar.

2.2. Synthesis of Co_1Fe_x LDH

$Co(NO_3)_2{\cdot}6H_2O$ (1 mmol) and $FeCl_3{\cdot}6H_2O$ (x = 0.1, 0.2, 0.3, 0.4 and 0.5 mmol) were dissolved into 100 mL of DIW (contains 1 g Pluronic P123) at room temperature. After stirring for 20 min, $NaBH_4$ (the molar ratio of $NaBH_4$/M was 1.5) was added and continuously stirred for 1 h. Subsequently, the precipitate was washed with DIW and C_2H_5OH alternately for three times. After vacuum drying, the synthesized samples were named Co_1Fe_x LDH, where x represented the molar ratio of Fe/Co (x = 0.1, 0.2, 0.3, 0.4 and 0.5).

2.3. Synthesis of $Co_1Fe_{0.2}$ NPs

$Co_1Fe_{0.2}$ NPs were synthesis similarly to Co_1Fe_x LDH except that Pluronic P123 was not added.

2.4. Synthesis of Fe LH and Co LH

Fe LH and Co LH were prepared by the same way as Co_1Fe_x LDH with only $FeCl_3{\cdot}6H_2O$ and $Co(NO_3)_2{\cdot}6H_2O$ as the metal precursor, respectively.

2.5. Characterization

High-resolution TEM (HRTEM) images were recorded on a JEM-2100 transmission electron microscope (Tokyo, Japan) at 200 kV. The valence state was determined using XPS recorded on a Thermo ESCALAB 250Xi. The X-ray source selected was monochromatized Al K_α source (15 kV, 10.8 mA). Region scans were collected using a 30 eV pass energy. Peak positions were calibrated relative to C 1*s* peak position at 284.6 eV.

2.6. X-ray absorption data collection

The X-ray absorption fine structure (XAFS) spectra were performed at BL14W1 beamline of Shanghai Synchrotron Radiation Facility (SSRF) operated at 3.5 GeV under "top-up" mode with a constant current of 240 mA. The XAFS data were recorded under fluorescence mode with a 7-element Ge solid state detector. The energy was calibrated accordingly to the absorption edge of Fe/Co foil. Athena and Artemis codes were used to extract the data and fit the profiles. For the X-ray absorption near edge structure (XANES) part, the experimental absorption coefficients as function of energies $\mu(E)$ were processed by background subtraction and normalization procedures, and reported as "normalized absorption". For the extended X-ray absorption fine structure (EXAFS) part, the Fourier transformed (FT) data in R space were analyzed by applying first-shell approximate model for Fe-O and Co-O contributions. The parameters describing the electronic properties (e.g.,

(C)1994-2023 China Academic Journal Electronic Publishing House. All rights reserved. http://www.cnki.net

correction to the photoelectron energy origin, E_0) and local structure environment including CN, bond distance (R) and Debye-Waller (D.W.) factor around the absorbing atoms were allowed to vary during the fit process. The fitted range for k space was selected to be k = 3–10 Å^{-1} (k^3 weighted).

2.7. Electrochemical measurements

All electrochemical measurements were performed on a CHI760E electrochemical working station at room temperature. The catalysts were measured in 1.0 mol/L KOH aqueous solution using a typical three-electrode configuration, in which glassy carbon electrode (GCE) was used as the working electrode; platinum plate and saturated calomel electrode (SCE, saturated KCl) were used as the counter and reference electrodes, respectively. Linear sweep voltammetry (LSV) polarization curves were acquired at a scan rate of 1 mV s^{-1} with 90% *i*R-compensation. Electrochemical impedance spectroscopy (EIS) measurements were performed at open-circuit potential in the frequency range from 100 kHz to 0.1 Hz with an a.c. perturbation of 5 mV. All potentials measured were calibrated to RHE using the following equation: E (*vs*. RHE) = E (*vs*. SCE) + 0.241V + 0.0591pH.

Typically, 2 mg of catalyst powder was dispersed in 0.5 ml ethanol containing 0.25 wt% Nafion solution. The suspension was immersed in an ultrasonic bath for 30 min to prepare a homogeneous ink. The working electrode was prepared by depositing 5 μl catalyst ink onto GCE (catalyst loading 0.28 mg cm^{-2}).

2.8. Computational methods

Spin-polarized DFT calculations were performed using the Vienna Ab initio Simulation Package. The generalized gradient approximation with the PBE functional was used to describe the exchange and correlation energy. Electron–ion interactions were treated by the projector augmented wave method. In all calculations, the energy cutoff of the plane-wave basis set was 400 eV. The DFT+U method was applied to 3*d* orbitals of Fe and Co to correct the on-site Coulomb interactions. U_{eff} = 5 eV and 3.4 eV were used respectively for Fe and Co to reproduce the electronic structure that has been observed experimentally. Brillouin zone was sampled by Monkhorst-Pack k-point meshes. Optimized structures were obtained by minimizing the forces on each ion until they fell below 0.05 eV/Å. The solvation effects were also considered using an implicit solvation model implemented in VASP. The relative permittivity for the continuum solvent was set to 80 to simulate a water environment.

Thermochemistry of the electrochemical oxygen evolution reaction (OER) was calculated by applying the computational hydrogen electrode method. This method has previously proved successful in predicting OER activity trends on various catalysts. Briefly, the Gibbs free energy change of each electrochemical elementary step of the OER was calculated with DFT. The OER reaction mechanism was assumed to follow the four-step mechanism represented in equations 1–4.

$$H_2O + * \leftrightarrow OH^* + H^+ + e^- \quad (1)$$

$$OH^* \leftrightarrow O^* + H^+ + e^- \quad (2)$$

$$H_2O + O^* \leftrightarrow OOH^* + H^+ + e^- \quad (3)$$

$$OOH^* \leftrightarrow * + O_2 + H^+ + e^- \quad (4)$$

The free energy change of each elementary steps can be calculated as $\Delta G = \Delta E - T\Delta S + \Delta ZPE$, where ΔZPE is the zero-point energy. The total energy changes (ΔE) of these elementary steps are the energy differences between DFT-calculated energies of reactant and product states. Here, for both ORR and OER, we evaluated the binding energies of OH*, O*, and OOH* on the surfaces of the catalysts under consideration. The chemical potential of the solvated proton and electron pair ($H^+ + e^-$) at standard conditions (pH = 0, T = 298.15 K) is calculated as $1/2G_{H2} + eU_{SHE}$ assuming equilibrium at the standard hydrogen electrode. The changes in ΔZPE and $T\Delta S$ are calculated using previously determined values. With this approach, the theoretical overpotential of OER (η^{OER}) at standard conditions is defined as:

$$\eta^{OER} = (G^{OER}/e) - 1.23V \quad (5),$$

where G^{OER} is the potential determining step defined as the highest free energy step in the process of OER.

We employed b-CoOOH(01-12) and γ-FeOOH(010) surfaces to examine their OER activities, respectively. A vacuum spacing of at least 20 Å was used for all surface models. All surface structural models had a minimum of four metal-oxygen layers and 3 × 3 cell sampled by 2 × 2 × 1 Monkhorst-Pack [8] k-point mesh. For Fe-doped CoOOH(01-12) surface, we explored two different doping locations of Fe dopants. The first location is Fe dopant replaces a surface Co on CoOOH surface. And, the second is Fe dopant occupy a subsurface lattice of CoOOH. The OER activities of the surface Fe along with the Co sites adjacent to the Fe dopants were examined.

3. Results and discussion

3.1. Morphology and structure characterization

CoFe LDH was facilely synthesized using a template-assist method at room temperature. Fig. 1(a) shows the ultrathin CoFe LDH nanosheets with different Co/Fe concentrations fabricated via a two-step process. In the first step, Fe^{3+} ions, Co^{2+} ions, and polyethylene oxide-polypropylene oxide-polyethylene oxide (P123) were dissolved in water with stirring. In the second step, sodium borohydride was added to precipitate the metal ions and form the ultrathin 2D structure. High-resolution transmission electron microscopy (HRTEM) images (Figs. 1(b) and (c)) present the 2D layered structure of the $Co_1Fe_{0.2}$ LDH. The structure was wrinkled and < 2-nm thick. The HRTEM image (Fig. 1(c)) presents typical crystal lattices with a spacing of 0.462 nm, which is slightly larger than the (001) plane spacing of $Fe(OH)_2$ (0.46 nm, PDF#13-0089) and the (001) plane spacing of FeOOH (0.456 nm, PDF#77-0247) but smaller than the (001) plane spacing of $Co(OH)_2$ (0.464 nm, PDF#74-1057). This finding suggests that iron ions were successfully immobilized in the $Co(OH)_2$ lattice. The peaks shown in the X-ray diffraction (XRD) pattern of Co_1Fe_x LDH are considerably shifted from the corresponding peaks of FeOOH and $Co(OH)_2$ (Fig. S1), further demonstrating the formation of bi-

(C)1994-2023 China Academic Journal Electronic Publishing House. All rights reserved. http://www.cnki.net

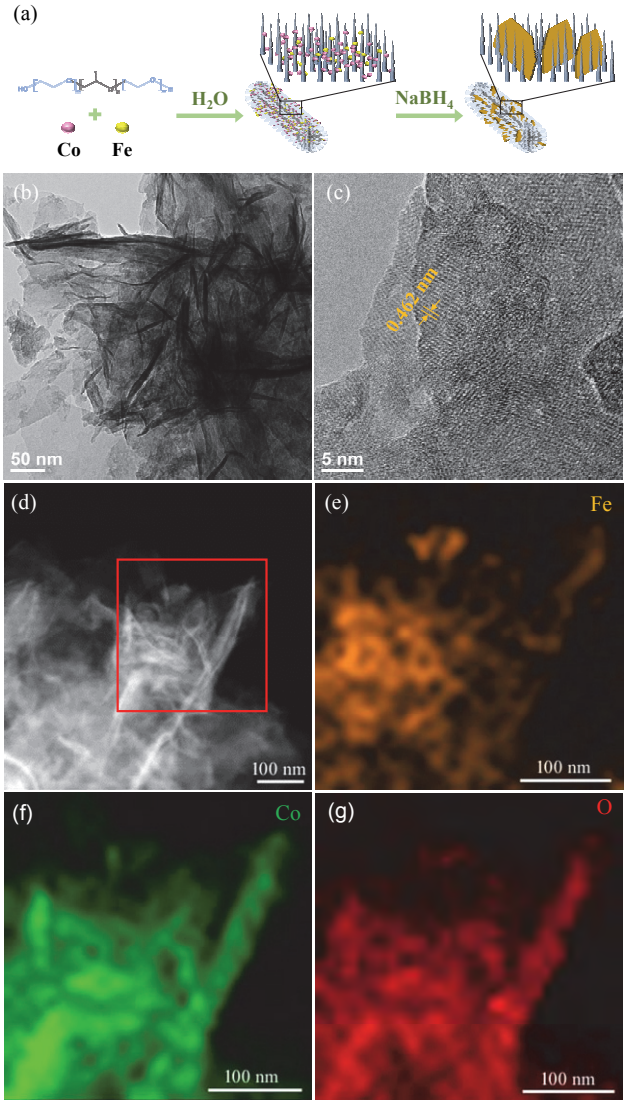

Fig. 1. (a) Schematic of the process of synthesizing CoFe LDH; HRTEM images (b–d) and EDX mappings (e–g) of the $Co_1Fe_{0.2}$ LDH.

metallic hydroxides. Energy dispersive X-ray spectroscopy (EDX) and elemental mapping images confirm the uniform dispersion of Fe, Co, and O (Figs. 1(d)–(g)). From the nitrogen adsorption-desorption isotherms, the Brunauer-Emmett-Teller specific surface area of Co_1Fe_x LDH was determined as 97.7 $m^2 g^{-1}$.

Surface-sensitive X-ray photoelectron spectroscopy (XPS) and synchrotron-based XAFS are effective characterization techniques for determining the surfaces and bond structures of active metal sites. First, the chemical nature of the as-prepared $Co_1Fe_{0.2}$ LDH was investigated using XPS. The survey spectrum (Fig. 2(a)) presents clear peaks of C 1*s*, O 1*s*, Fe 2*p*, and Co 2*p*. At high resolution, the Fe 2*p* peak splits into Fe $2p_{3/2}$ (713.6 eV) and Fe $2p_{1/2}$ (724.7 eV) along with two satellite peaks, one located at 718.8 eV and the other at 734.2 eV (Fig. 2(b)). The Fe $2p_{3/2}$ and Fe $2p_{1/2}$ peaks are deconvolved into Fe^{2+} $2p_{3/2}$ (710.9 eV), Fe^{3+} $2p_{3/2}$ (713.1 eV), Fe^{2+} $2p_{1/2}$ (724.1 eV), and Fe^{3+} $2p_{1/2}$ (726.1 eV) [30]. From the peak areas, the surface content of Fe^{3+}/Fe^{2+} is calculated as ca. 9/1. In the high-resolution Co 2*p* spectrum of the $Co_1Fe_{0.2}$ LDH (Fig. 2(c)), two prominent shake-up satellite peaks centered at 786.6 and 803.2 eV indicate the existence of Co^{2+} [31]. The two major peaks centered at ~781.5 and 797.5 eV (split by ~16 eV) are attributed to the Co $2p_{3/2}$ and Co $2p_{1/2}$ orbitals, respectively. These peaks were further deconvolved into Co^{2+} $2p_{3/2}$ (781.5 eV), Co^{3+} $2p_{3/2}$ (779.9 eV), Co^{2+} $2p_{1/2}$ (797.5 eV), and Co^{3+} $2p_{1/2}$ (795.9 eV) [32]. The surface relative content of Co^{3+}/Co^{2+} is ca. 1/7.4. In the O 1*s* spectrum (Fig. 2(d)), the peaks at 529.8, 531.4, and 532.5 eV are attributed to lattice oxygen (Fe/Co-O), defective oxygen sites, and surface-absorbed –OH, respectively [22,33–35].

The local coordination structures of the Fe and Co species in the $Co_1Fe_{0.2}$ LDH were thoroughly determined using XAFS measurements (Fig. 3). First, the oxidation states of the Fe and Co ions were confirmed *via* X-ray absorption near-edge structure (XANES) spectroscopy. In the Fe K-edge of the XANES spectra, the near-edge structures of the $Co_1Fe_{0.2}$ LDH and Fe_2O_3 were very similar (Fig. 3(a)), indicating an average valence state of +3 for Fe. The Co K-edge of the XANES spectra of the $Co_1Fe_{0.2}$ LDH appeared between those of CoO and Co_3O_4 (Fig. 3(d)), indicating an average valence state of Co between +2 and +3. Both XANES results agreed with the aforementioned XPS results. Subsequently, the local structures of the Fe and Co sites in the $Co_1Fe_{0.2}$ LDH were analyzed using extended X-ray fine structure (EXAFS) spectroscopy (Figs. 3(b) and 3(e)). The Fourier-transformed (FT) EXAFS spectra are displayed in Figs. 3(c) and 3(f), and the extracted structural parameters are presented in Table S1. The Fe atomic environment of the $Co_1Fe_{0.2}$ LDH has O in the first shell with a bond length of 1.98 ± 0.01 Å and an average coordination number of 5.7 ± 0.7. Fe/Co occupies the second coordination shell with a distance of 3.09 ± 0.02 Å. Meanwhile, the Co atomic environment of the $Co_1Fe_{0.2}$ LDH has O in the first shell with a bond length of 2.05 ± 0.01 Å and an average coordination number of 6.8 ± 0.9. Fe/Co appears in the second coordination shell with a distance of 3.12 ± 0.01 Å.

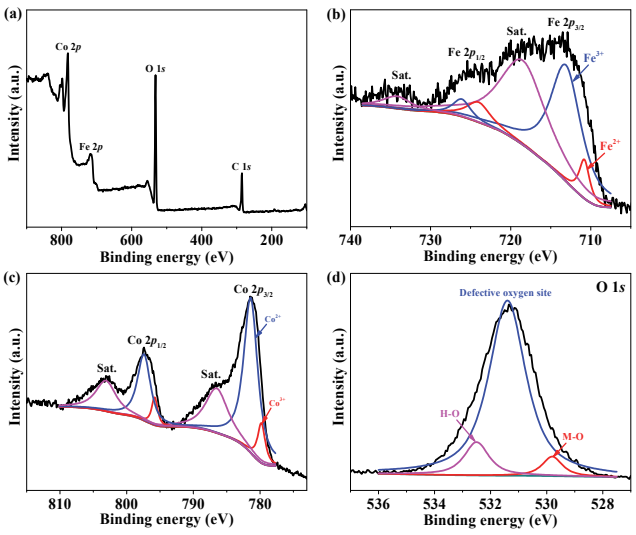

Fig. 2. (a) XPS survey spectrum of the $Co_1Fe_{0.2}$ LDH. (b) high-resolution Fe 2*p* XPS spectra. (c) high-resolution Co 2*p* XPS spectra. (d) high-resolution O 1*s* XPS spectra.

(C)1994-2023 China Academic Journal Electronic Publishing House. All rights reserved. http://www.cnki.net

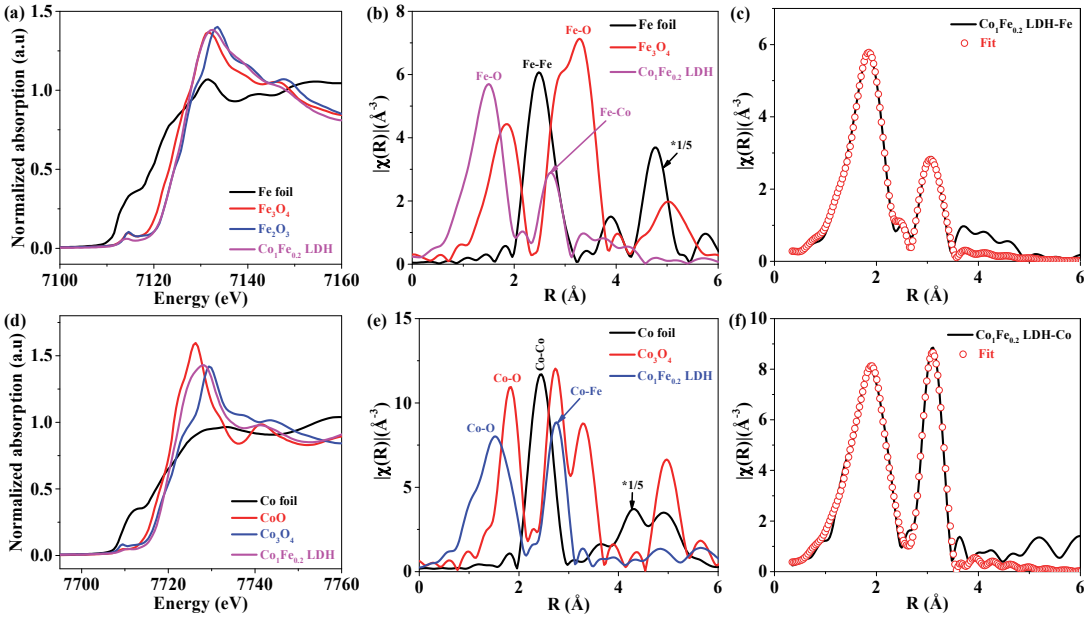

Fig. 3. (a) XANES spectra at the Fe K-edge of the $Co_1Fe_{0.2}$ LDH and reference samples (Fe foil, Fe_3O_4, and Fe_2O_3). (b) EXAFS spectra at the Fe K-edge of the $Co_1Fe_{0.2}$ LDH, Fe foil, and Fe_3O_4. (c) FT-EXAFS fitting spectrum at the Fe K-edge of $Co_1Fe_{0.2}$ LDH. (d) XANES spectra at the Co K-edge of the $Co_1Fe_{0.2}$ LDH and reference samples (Co foil, CoO, and Co_3O_4). (e) EXAFS spectra at the Co K-edge of the $Co_1Fe_{0.2}$ LDH, Co foil, and Co_3O_4. (f) FT-EXAFS fitting spectrum at the Co K-edge of $Co_1Fe_{0.2}$ LDH.

3.2. OER performance

The electrocatalytic OER performance of the as-prepared $Co_1Fe_{0.2}$ LDH was evaluated in an alkaline electrolyte using a standard three-electrode system (Fig. 4). For comparison, Fe layer hydroxide (Fe LH), Co layer hydroxide (Co LH), $Co_1Fe_{0.2}(OH)_x$ NPs ($Co_1Fe_{0.2}$ NPs), and commercial IrO_2 were tested under the same condition. The linear sweep voltammetry curves were obtained at a scan rate of 1 mV s^{-1} with 90% iR compensation. Fig. S2 shows that the OER activity can be optimized by modulating the molar ratio of Co/Fe. The $Co_1Fe_{0.2}$ LDH showed excellent OER activity, achieving a current density (j) of 10 mA cm^{-2} at a lower overpotential (η_{10} = 256 mV) than those of $Co_1Fe_{0.1}$ LDH (265 mV), $Co_1Fe_{0.3}$ LDH (269 mV), $Co_1Fe_{0.4}$ LDH (277 mV), $Co_1Fe_{0.5}$ LDH (277 mV), and commercial IrO_2 (272 mV) (Fig. 4(a)). By contrast, the η_{10} values of Co LH and $Co_1Fe_{0.2}$ NPs were 307 and 292 mV, respectively and Fe LH failed to reach the current density of 10 mA cm^{-2} even when the overpotential reached 700 mV. The considerable down shift in the overpotential from Co LH to CoFe LDH strongly indicates that a cooperation mechanism between Fe and Co plays a vital role in the OER. Furthermore, the $Co_1Fe_{0.2}$ LDH exhibited a high turnover frequency of 0.082 s^{-1} per total 3d metal atoms and a mass activity of 277.9 A g^{-1} at an overpotential of 300 mV, which are much higher than those of Fe LH (0.00019 s^{-1} and 0.58 A g^{-1}, respectively), Co LH (0.0085 s^{-1} and 29.6 A g^{-1}, respectively), $Co_1Fe_{0.2}$ NPs (0.015 s^{-1} and 51.1 A g^{-1}, respectively), and IrO_2 (0.077 s^{-1} and 111.4 A g^{-1}, respectively) [23]. The $Co_1Fe_{0.2}$ LDH conformably surpassed the best CoFe-based LDH electrocatalysts previously reported (Fig. 4(c)); for example Fe-CoOOH/G (η_{10} = 330 mV) [36], CoFe LDH/rGO (η_{10} = 325 mV) [37], α-$Co_4Fe(OH)_x$ (η_{10} = 295 mV) [38], CoFe LDH (η_{10} = 288 mV) [39], α-$Co_{0.9}Fe_{0.1}(OH)_x$ (η_{10} = 280 mV) [40], Co-Fe oxyphosphide microtubes (η_{10} = 280 mV) [41], $(CoFe)(OH)_x$ (η_{10} = 275 mV) [42], CoFe LDHs-Ar (η_{10} = 266 mV) [43], $Fe_{0.33}Co_{0.67}OOH$ porous nanosheet arrays grown on carbon fiber cloth (η_{10} = 266 mV) [44], and CoFe metal-organic framework (η_{10} = 265 mV) [45].

To further investigate the OER performance, Tafel plots were derived from the polarization curves of the catalysts. The Tafel slope of the $Co_1Fe_{0.2}$ LDH is 40 mV dec^{-1} (Fig. 4(b)), implying that second electron transfer is the potential-determining step for the OER [46]. By contrast, the similar Tafel slopes of $Co_1Fe_{0.2}$ NPs and commercial IrO_2 are 67 and 58 mV dec^{-1}, respectively, implying that the OER's potential-determining step is the step following the first electron transfer. The much lower Tafel slope of Co LH (92 mV dec^{-1}) demonstrates a different mechanism from those of the $Co_1Fe_{0.2}$ LDH and $Co_1Fe_{0.2}$ NPs, further indicating that the introduced Fe changed the water-oxidation-reaction route on the catalyst surface. The doping content of Fe in the CoFe LDH also influenced the OER mechanism (Fig. S2), suggesting that finding an appropriate Co/Fe ratio is essential for improving the OER performance of catalysts.

To assess the OER kinetic barrier, we investigated the influence of temperature on the electrocatalytic performances of the catalysts. Raising the temperature accelerated the water-oxidation process (Fig. S3), indicating that the electrochemical rate constant is temperature dependent. From the Arrhenius plots at η = 300 mV, the OER activation energy (E_a) was determined as $E_a = -2.3R[\partial\log(i_k)/\partial 1/T]$ (Fig. 4(c)), where i_k is the kinetic current at η = 300 mV, T is the temperature, and R is the universal gas constant [23,47]. The apparent energy

(C)1994-2023 China Academic Journal Electronic Publishing House. All rights reserved. http://www.cnki.net

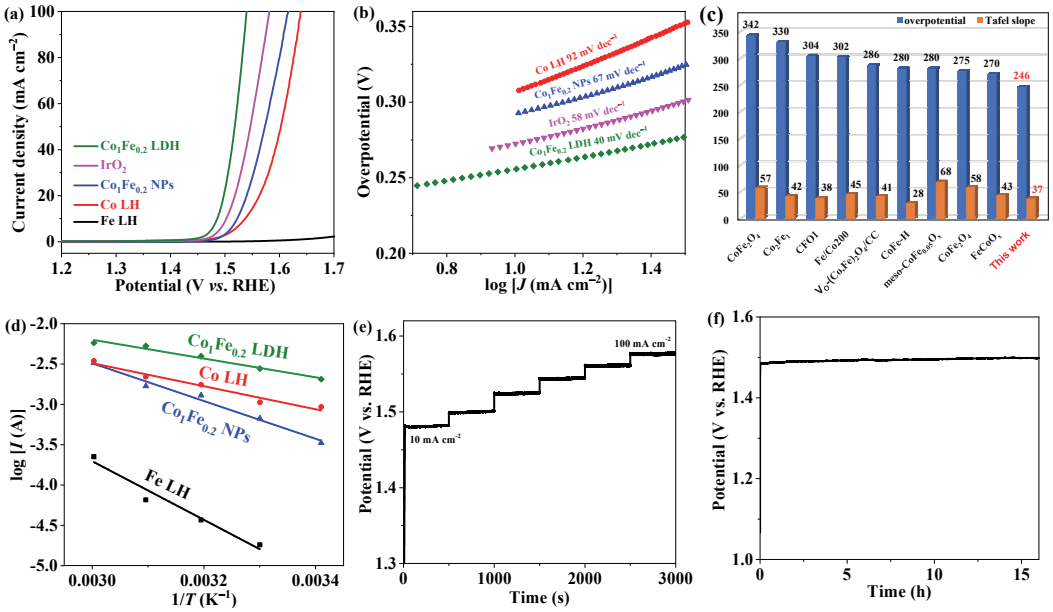

Fig. 4. (a) OER polarization curves of the catalysts loaded on the glassy carbon electrodes. Tafel slopes (b) and comparisons (c) of the overpotentials at 10 mA cm^{-2} and Tafel slopes of the catalysts. (d) Arrhenius plots of the kinetic current at η = 300 mV without *i*R compensation. (e) Multicurrent electrochemical process and (f) chronopotentiometric curve of the Co$_1$Fe$_{0.2}$ LDH.

barrier was much lower in the Co$_1$Fe$_{0.2}$ LDH (22.2 kJ mol^{-1}) than in Fe LH (69.6 kJ mol^{-1}), Co LH (27.3 kJ mol^{-1}), and Co$_1$Fe$_{0.2}$ NPs (44.8 kJ mol^{-1}), suggesting faster OER kinetics on the Co$_1$Fe$_{0.2}$ LDH than on the other catalysts. However, Co LH showed a lower activation energy than those of Fe LH and Co$_1$Fe$_{0.2}$ NPs, implying that Co sites are the main active centers for the OER.

To better estimate the available active sites for the OER, the electrochemically active surface area (ECSA) was derived from the electrochemical double-layer capacitance [48]. The ECSAs of Fe LH, Co LH, Co$_1$Fe$_{0.2}$ NPs, and the Co$_1$Fe$_{0.2}$ LDH were 2.9, 1888, 810, and 2625 cm^2 (Figs. S4–S7), respectively, suggesting that the high ECSA of Co$_1$Fe$_{0.2}$ LDH is mainly based on Co LH rather than Fe LH. Moreover, layered hydroxides exhibit higher ECSAs than NPs because the 2D ultrathin structure exposes more active sites. Then, an impedance study was performed to determine the nature of the electrode surface and its role in the electrocatalytic OER. As shown by the Nyquist plots presented in Fig. S8, the charge-transfer resistance was much lower in the Co$_1$Fe$_{0.2}$ LDH than in Fe LH, Co LH, and Co$_1$Fe$_{0.2}$ NPs, implying a faster charge-transfer capability of the Co$_1$Fe$_{0.2}$ LDH than those of the other catalysts during the OER.

To study the steady-state activity and durability of the Co$_1$Fe$_{0.2}$ LDH, multiple current steps of chronopotentiometry were performed in an alkaline electrolyte. Fig. 4(e) shows that the overpotential remains almost constant as the current density increases stepwise from 10 to 100 mA cm^{-2}. The roughening of the plots at high current densities is attributable to oxygen-bubble formation during the OER. The OER durability of the Co$_1$Fe$_{0.2}$ LDH was further investigated at constant current density of 10 mA cm^{-2} for 16 h (Fig. 4(f)). The excellent stability of the Co$_1$Fe$_{0.2}$ LDH was confirmed by the steady OER activity over the 16-h period.

The morphology and structure of the Co$_1$Fe$_{0.2}$ LDH after the OER test were analyzed using TEM and XRD, respectively. As shown in the TEM image (Fig. S9), the typical nanosheet structure of the Co$_1$Fe$_{0.2}$ LDH was preserved after the OER test, indicating that the morphology was not disrupted by the OER. Meanwhile, the XRD pattern of the Co$_1$Fe$_{0.2}$ LDH after the OER test (Fig. S10) presents obvious peaks of bimetallic Co-Fe hydroxide, indicating that the structure of the Co$_1$Fe$_{0.2}$ LDH was well retained during the OER. The changes in the composition and valence states of Co and Fe on the Co$_1$Fe$_{0.2}$ LDH surface after the OER stability test were determined via XPS. The Co and Fe compositions did not seem to change after the OER test (Fig. S11), further suggesting the high stability of the Co$_1$Fe$_{0.2}$ LDH. The relative surface contents of Fe^{3+}/Fe^{2+} and Co^{3+}/Co^{2+} increased from 9/1 and 1/7.4 in the fresh sample to 10/1 and 1/6.3, respectively, in the used sample, indicating that the surface Fe and Co sites are involved in the OER process.

3.3. OER mechanism

To rationalize the effect of Fe doping on the OER activity of CoOOH, we evaluated the theoretical OER overpotential (η_{OER}) of unary CoOOH, FeOOH, and binary Fe-CoOOH catalysts using density functional theory with the Hubbard U correction. For the binary Fe-CoOOH catalyst, we considered both surface and subsurface Fe alloying. In the former case, the OER performance was determined at the surface Fe sites (Fe-CoOOH Fe) and at Co sites adjacent to the Fe dopants (Fe-CoOOH Co). In the latter case, the OER performance was determined at the surface Co sites above the subsurface Fe dopants (Fe$_{sub}$-CoOOH Co). The theoretical OER overpotentials at these five catalytic

(C)1994-2023 China Academic Journal Electronic Publishing House. All rights reserved. http://www.cnki.net

sites were calculated according to the proposed four-step OER mechanism in an alkaline media. The proposed mechanism is shown in Fig. 5(a), and the calculated OER overpotentials are plotted against the thermochemical descriptor of OER activity, i.e., $\Delta G_O - \Delta G_{OH}$, as shown in Fig. 5(b). The overpotentials of the examined cases are overlaid with the theoretical volcano plot (Fig. 5(b)). The detailed free-energy diagrams (FEDs) of the OER constructed from the energetics of all intermediates (OH*, O*, and OOH*) at different applied potentials at the five catalytic sites are shown in Figs. 5(c)–(g). The poor activity of the FeOOH site for the OER with a high η_{OER} (~0.95 V) can be attributed to the excessively strong bonding of OH*. The OER activity of CoOOH was much higher (η_{OER} ~0.7 V) because the adsorption strengths of the key reaction intermediates were better balanced at this site. However, the stronger absorption of OH* than that of O* raised the overpotential of the OH* to O* for the oxidation step. For this reason, the data point of CoOOH is located toward the right side of the optimal point on the volcano plot shown in Fig. 5(b). We found that the CoOOH site was improved via surface Fe doping. Specifically, the OER overpotential at a Co site adjacent to a surface Fe dopant fell to ~0.61 V. This improvement can be attributed to slightly more destabilized OH* adsorption than that on unary CoOOH. However, the subsurface Fe dopant excessively weakened the OH* adsorption; accordingly, the $\Delta G_O - \Delta G_{OH}$ value appeared to the left side of its optimal value on the volcano plot and the OER activity decreased at the Co site above the subsurface Fe dopant. Finally, we examined a surface Fe site; however, its activity was lower than that of unary CoOOH. Overall, we concluded that surface Fe doping enhanced the OER activity of CoOOH by moderately destabilizing the OH* bonding. The calculated results were well consistent with the aforementioned experimental findings. First, the kinetic studies confirmed the Co site as the main active center for the OER, as theoretically predicted. Second, the ultrathin 2D nanosheets of the $Co_1Fe_{0.2}$ LDH exposed numerous Fe and Co surface sites and increased the number of Co sites adjacent to Fe atoms. Finally, as FeOOH has poor electrical conductivity, increasing the surface doping by adding Fe atoms into the $Co_1Fe_{0.2}$ LDH improved the charge-transfer ability more compared with when more Fe atoms were doped into the bulk of $Co_1Fe_{0.2}$ NPs, thus facilitating the OER kinetics. These findings support that *di*-μ-oxo-bridged Co-Co and *di*-μ-oxo-bridged Fe-Co sites are the reaction centers for the OER, as previously reported. [28] Here, we emphasize that the main active sites are probably Co atoms. Our study provides more details on the location of di-μ-oxo-bridged Fe-Co sites that should present at the CoFe LDH surface.

4. Conclusions

In summary, we report a simple solution-reaction method for preparing ultrathin $Co_1Fe_{0.2}$ LDH nanosheets for an efficient OER. The $Co_1Fe_{0.2}$ LDH nanosheets require an overpotential of only 256 mV at 10 mA cm^{-2}, which is superior to those of commercial IrO_2 and most of the best-performing electrocatalysts reported previously. The excellent OER performance of the $Co_1Fe_{0.2}$ LDH is attributed to the ultrathin 2D nanosheets, which provide abundant active sites and excellent charge-transfer ability. Kinetic studies reveal that Co sites are the main active centers for the OER on the $Co_1Fe_{0.2}$ LDH while the Fe dopant lowers the reaction barrier. Theoretical calculations confirm that the lowest overpotential appeared on the

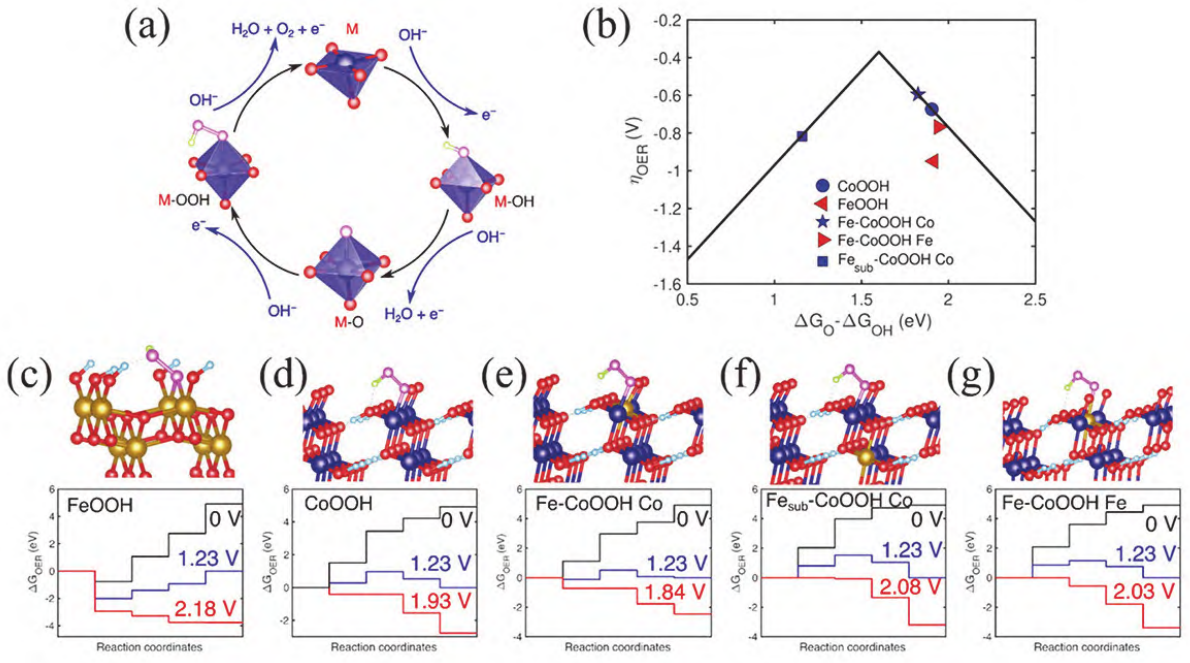

Fig. 5. (a) OER mechanism over a metal-oxide surface site M in an alkaline solution. (b) Predicted overpotentials (η_{OER}) over various catalytic sites overlaid on a theoretical volcano plot of the OER; Free-energy diagrams (FEDs) of the OER using FeOOH (c), CoOOH (d), Fe-CoOOH Co (e), Fe_{sub}-CoOOH Co (f), and Fe-CoOOH Co (g) sites. The atomic models of OOH adsorbed on these sites are shown above their respective FEDs. The brown, blue, red/pink, and green balls represent Fe, Co, O, and H atoms, respectively.

(C)1994-2023 China Academic Journal Electronic Publishing House. All rights reserved. http://www.cnki.net

surface Co sites adjacent to the Fe atoms. Therefore, these surface Co centers are the expected active sites for the OER.

Electronic supporting information

Supporting information is available in the online version of this article.

References

[1] C. Guo, Y. Shi, S. Lu, Y. Yu, B. Zhang, *Chin. J. Catal.*, **2021**, 42, 1287–1296.
[2] Z. Li, M. Hu, P. Wang, J. Liu, J. Yao, C. Li, *Coord. Chem. Rev.*, **2021**, 439, 213953.
[3] Q. Xu, J. Zhang, H. Zhang, L. Zhang, L. Chen, Y. Hu, H. Jiang, C. Li, *Energy Environ. Sci.*, **2021**, 14, 5228–5259.
[4] J. Yin, J. Jin, H. Zhang, M. Lu, Y. Peng, B. Huang, P. Xi, C.-H. Yan, *Angew. Chem. Int. Ed.*, **2019**, 58, 18676–18682.
[5] S. Li, J. Sun, J. Guan, *Chin. J. Catal.*, **2021**, 42, 511–556.
[6] Z.-Y. Yu, Y. Duan, X.-Y. Feng, X. Yu, M.-R. Gao, S.-H. Yu, *Adv. Mater.*, **2021**, 33, 2007100.
[7] G. M. Tomboc, J. Kim, Y. Wang, Y. Son, J. Li, J. Y. Kim, K. Lee, *J. Mater. Chem. A*, **2021**, 9, 4528–4557.
[8] J. Yin, J. Jin, H. Liu, B. Huang, M. Lu, J. Li, H. Liu, H. Zhang, Y. Peng, P. Xi, C.-H. Yan, *Adv. Mater.*, **2020**, 32, 2001651.
[9] D. Liu, A. Barbar, T. Najam, M. S. Javed, J. Shen, P. Tsiakaras, X. Cai, *Appl. Catal. B*, **2021**, 297, 120389
[10] J. Guan, X. Bai, T. Tang, *Nano Res.*, **2022**, 15, 818–837.
[11] H. Sun, X. Xu, Y. Song, W. Zhou, Z. Shao, *Adv. Funct. Mater.*, **2021**, 31, 2009779.
[12] P. M. Bodhankar, P. B. Sarawade, G. Singh, A. Vinu, D. S. Dhawale, *J. Mater. Chem. A*, **2021**, 9, 3180–3208.
[13] L. An, C. Wei, M. Lu, H. Liu, Y. Chen, G. G. Scherer, A. C. Fisher, P. Xi, Z. J. Xu, C.-H. Yan, *Adv. Mater.*, **2021**, 33, 2006328.
[14] S. Anantharaj, S. R. Ede, K. Sakthikumar, K. Karthick, S. Mishra, S. Kundu, *ACS Catal.*, **2016**, 6, 8069–8097.
[15] H. Jin, C. Guo, X. Liu, J. Liu, A. Vasileff, Y. Jiao, Y. Zheng, S.-Z. Qiao, *Chem. Rev.*, **2018**, 118, 6337–6408.
[16] M.-R. Gao, Y.-F. Xu, J. Jiang, S.-H. Yu, *Chem. Soc. Rev.*, **2013**, 42, 2986–3017.
[17] L. Zhang, J. Xiao, H. Wang, M. Shao, *ACS Catal.*, **2017**, 7, 7855–7865.
[18] C. Hu, L. Dai, *Adv. Mater.*, **2017**, 29, 1604942.
[19] C. C. L. McCrory, S. Jung, I. M. Ferrer, S. M. Chatman, J. C. Peters, T. F. Jaramillo, *J. Am. Chem. Soc.*, **2015**, 137, 4347–4357.
[20] A. Kargar, S. Yavuz, T. K. Kim, C.-H. Liu, C. Kuru, C. S. Rustomji, S. Jin, P. R. Bandaru, *ACS Appl. Mater. Interfaces*, **2015**, 7, 17851–17856.
[21] L. Zhuang, L. Ge, Y. Yang, M. Li, Y. Jia, X. Yao, Z. Zhu, *Adv. Mater.*, **2017**, 29, 1606793.
[22] N. Liu, J. Guan, *Mater. Today Energy*, **2021**, 21, 100715.
[23] B. Zhang, X. Zheng, O. Voznyy, R. Comin, M. Bajdich, M. García-Melchor, L. Han, J. Xu, M. Liu, L. Zheng, F. P. García de Arquer, C. T. Dinh, F. Fan, M. Yuan, E. Yassitepe, N. Chen, T. Regier, P. Liu, Y. Li, P. De Luna, A. Janmohamed, H. L. Xin, H. Yang, A. Vojvodic, E. H. Sargent, *Science*, **2016**, 352, 333–337.
[24] T. Tang, Q. Zhang, X. Bai, Z. Wang, J. Guan, *Chem. Commun.*, **2021**, 57, 11843–11846.
[25] F. Dionigi, J. Zhu, Z. Zeng, T. Merzdorf, H. Sarodnik, M. Gliech, L. Pan, W.-X. Li, J. Greeley, P. Strasser, *Angew. Chem. Int. Ed.*, **2021**, 60, 14446–14457.
[26] X. Zeng, M. J. Jang, S. M. Choi, H.-S. Cho, C.-H. Kim, N. V. Myung, Y. Yin, *Mater. Chem. Front.*, **2020**, 4, 2307–2313.
[27] L. Gong, X. Y. E. Chng, Y. Du, S. Xi, B. S. Yeo, *ACS Catal.*, **2018**, 8, 807–814.
[28] R. D. L. Smith, C. Pasquini, S. Loos, P. Chernev, K. Klingan, P. Kubella, M. R. Mohammadi, D. Gonzalez-Flores, H. Dau, *Nat. Commun.*, **2017**, 8, 2022.
[29] Y. Wang, C. Xie, Z. Zhang, D. Liu, R. Chen, S. Wang, *Adv. Funct. Mater.*, **2018**, 28, 1703363.
[30] H.-L. Wei, A.-D. Tan, S.-Z. Hu, J.-H. Piao, Z.-Y. Fu, *Chin. J. Catal.*, **2021**, 42, 1451–1458.
[31] K. Cao, L. Jiao, Y. Liu, H. Liu, Y. Wang, H. Yuan, *Adv. Funct. Mater.*, **2015**, 25, 1082–1089.
[32] X. Zhang, M. Jin, Q. Lian, O. Peng, S. Niu, Z. Ai, A. Amini, S. Song, C. Cheng, *Chem. Eng. J.*, **2021**, 423, 130218.
[33] C. Dong, X. Yuan, X. Wang, X. Liu, W. Dong, R. Wang, Y. Duan, F. Huang, *J. Mater. Chem. A*, **2016**, 4, 11292–11298.
[34] Q. Zhang, N. Liu, J. Guan, *ACS Appl. Energy Mater.*, **2019**, 2, 8903–8911.
[35] Y. Li, M. Lu, Y. Wu, Q. Ji, H. Xu, J. Gao, G. Qian, Q. Zhang, *J. Mater. Chem. A*, **2020**, 8, 18215–18219.

Graphical Abstract

Chin. J. Catal., 2022, 43: 2240–2248 doi: 10.1016/S1872-2067(21)64033-0

Unveiling the active sites of ultrathin Co-Fe layered double hydroxides for the oxygen evolution reaction

Xue Bai, Zhiyao Duan *, Bing Nan, Liming Wang, Tianmi Tang, Jingqi Guan *
Jilin University; Northwestern Polytechnical University; Shanghai Advanced Research Institute, Chinese Academy of Science; Institute of High Energy Physics, Chinese Academy of Sciences;

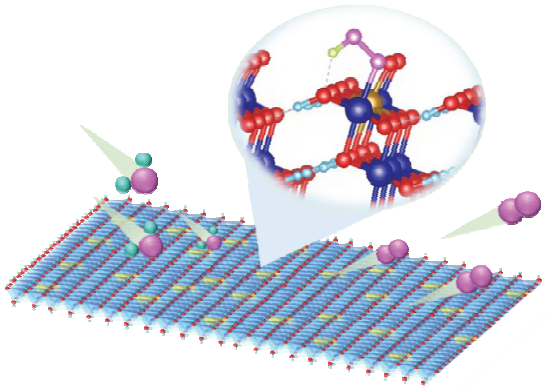

Ultrathin CoFe LDH displays a low overpotential (256 mV) at 10 mA cm^{-2}. The surface Co sites adjacent to Fe atoms are the active centers for the OER.

(C)1994-2023 China Academic Journal Electronic Publishing House. All rights reserved. http://www.cnki.net

[36] X. Han, C. Yu, S. Zhou, C. Zhao, H. Huang, J. Yang, Z. Liu, J. Zhao, J. Qiu, *Adv. Energy Mater.*, **2017**, 7, 1602148.
[37] X. Han, C. Yu, J. Yang, C. Zhao, H. Huang, Z. Liu, P. M. Ajayan, J. Qiu, *Adv. Mater. Interfaces*, **2016**, 3, 1500782.
[38] H. Jin, S. Mao, G. Zhan, F. Xu, X. Bao, Y. Wang, *J. Mater. Chem. A*, **2017**, 5, 1078–1084.
[39] Z. Li, M. Shao, H. An, Z. Wang, S. Xu, M. Wei, D. G. Evans, X. Duan, *Chem. Sci.*, **2015**, 6, 6624–6631.
[40] Y. Liu, M. Wang, Y. Li, G. Yuan, X. Zhang, Q. Wang, *ChemSusChem*, **2019**, 12, 2755–2762.
[41] P. Zhang, X. F. Lu, J. Nai, S.-Q. Zang, X. W. Lou, *Adv. Sci.*, **2019**, 6, 1900576.
[42] S. Liu, B. Liu, C. Gong, Z. Li, *Appl. Surf. Sci.*, **2019**, 478, 615–622.
[43] Y. Wang, Y. Zhang, Z. Liu, C. Xie, S. Feng, D. Liu, M. Shao, S. Wang, *Angew. Chem. Int. Ed.*, **2017**, 56, 5867–5871.
[44] S.-H. Ye, Z.-X. Shi, J.-X. Feng, Y.-X. Tong, G.-R. Li, *Angew. Chem. Int. Ed.*, **2018**, 57, 2672–2676.
[45] Z. Zou, T. Wang, X. Zhao, W.-J. Jiang, H. Pan, D. Gao, C. Xu, *ACS Catal.*, **2019**, 9, 7356–7364.
[46] M. S. Burke, M. G. Kast, L. Trotochaud, A. M. Smith, S. W. Boettcher, *J. Am. Chem. Soc.*, **2015**, 137, 3638–3648.
[47] J. R. Swierk, S. Klaus, L. Trotochaud, A. T. Bell, T. D. Tilley, *J. Phys. Chem. C*, **2015**, 119, 19022–19029.
[48] P. Zhang, L. Li, D. Nordlund, H. Chen, L. Fan, B. Zhang, X. Sheng, Q. Daniel, L. Sun, *Nat. Commun.*, **2018**, 9, 381.

揭示超薄Co-Fe层状双氢氧化物析氧反应的活性位点

白　雪[a,†], 段志遥[b,†,#], 南　兵[c,#], 王黎明[d], 唐甜蜜[a], 管景奇[*]
[a]吉林大学化学学院, 物理化学研究所, 吉林长春130021
[b]西北工业大学材料科学与工程学院, 凝固技术国家重点实验室, 陕西西安710072
[c]中国科学院上海高等研究院, 上海同步辐射光源, 上海201210
[d]中国科学院高能物理研究所, 中国科学院纳米生物效应与安全性重点实验室,
中国科学院-香港大学环境与健康金属组学联合实验室, 北京100049

摘要: 碱性条件下水分解生产高纯氢为能源的可持续发展提供了一条新途径. 然而电催化析氧反应(OER)需要克服高的能量势垒, 极大地影响了能源利用效率. Ir/Ru氧化物是一类性能优异的OER电催化剂, 但稀缺性和高成本限制了其大规模的工业化应用, 因此开发高性能且地球上资源丰富的元素来替代Ru/Ir氧化物有重要意义. 多相过渡金属氧化物、氢氧化物、碳化物、氮化物、卤化物、二卤化物、硒化物和磷化物只有高效的OER活性, 其中金属氧化物和氢氧化物的稳定性更好, 实际应用更广泛. 钴/铁基(氢)氧化物具有高的催化活性和稳定性, 可以构建成多种结构(包括纳米颗粒、纳米片、核-壳结构、介孔结构和结晶结构等)以提升其催化性能, 是一类能与贵金属氧化物相媲美的理想的OER电催化剂. 其中, 钴铁双金属氢氧化物(CoFe LDHs)由于其独特的二维结构和可调的化学组成, 在碱性介质中表现出良好的OER活性, 但其整体结构难以控制, 活性位点分布不均匀, 因此合理设计和制备具有超薄结构的CoFe LDHs, 提高电子传输速度是提高OER性能的关键.

本文采用一种简便的溶液反应制备CoFe基超薄双金属氢氧化物, 其厚度小于2 nm, 超薄的二维纳米片提供了丰富的OER活性位点和优异的电荷转移能力. 在1 mol/L KOH中, $Co_1Fe_{0.2}$ LDH仅需256 mV的过电位即可达到10 mA cm^{-2}的电流密度, 转化频率为0.082 s^{-1}, 在过电位为300 mV时, OER质量活性为277.9 A g^{-1}, 性能优于商用IrO_2, 也优于以往报道的大多数电催化剂. 动力学研究表明, Co位是OER的主要活性中心, 而掺杂Fe可以通过加速电荷转移过程降低反应势垒. 为了探究OER性能提高的机制, 对一元CoOOH, FeOOH和二元Fe-CoOOH上的五个不同位点进行了理论研究, 计算了它们在碱性介质中的理论OER过电位. 其中一元CoOOH中的Co位(0.95 V)的理论OER过电位比FeOOH的Fe位(0.7 V)低, 而二元Fe-CoOOH表面Fe原子附近的Co原子位点的理论OER过电位为0.61 V, 位于火山图的最顶端. 计算结果与实验相符, 表面Fe原子附近的Co位是OER的活性中心, 而次表面Fe的掺杂使OH*吸附作用过弱, 从而增加了速率决定步骤的能垒. 综上, 本文对合理设计高性能CoFe基水分解催化剂具有一定的参考意义.

关键词: 氢氧化钴; 氢氧化铁; 层状双氢氧化物; 析氧反应; 第一性原理研究

收稿日期: 2021-12-28. 接受日期: 2022-01-31. 上网时间: 2022-06-20.
*通讯联系人. 电子信箱: guanjq@jlu.edu.cn
#通讯联系人. 电子信箱: zhiyao.duan@nwpu.edu.cn
†共同第一作者.
基金来源: 国家自然科学基金(22075099); 吉林省教育厅(JJKH20220967KJ); 中央高校基本研究经费(D5000210743).
本文的电子版全文由Elsevier出版社在ScienceDirect上出版(http://www.sciencedirect.com/journal/chinese-journal-of-catalysis).

(C)1994-2023 China Academic Journal Electronic Publishing House. All rights reserved. http://www.cnki.net